Structure inversion asymmetry enhanced electronic structure and electrical transport in 2D A3SnO (A = Ca, Sr, and Ba) anti-perovskite monolayers

Alay-e-Abbas, Syed Muhammad; Abbas, Ghulam; Zulfiqar, Waqas; Sajjad, Muhammad; Singh, Nirpendra; Larsson, J. Andreas

Published in:
Nano Research

DOI:
10.1007/s12274-022-4637-3

Publication date:
2023

Document Version
Publisher's PDF, also known as Version of record

Nano Research
2023, 16(1): 1779–1791

ISSN 1998-0124 CN 11-5974/O4
https://doi.org/10.1007/s12274-022-4637-3

Research Article

Structure inversion asymmetry enhanced electronic structure and electrical transport in 2D A_3SnO (A = Ca, Sr, and Ba) anti-perovskite monolayers

Syed Muhammad Alay-e-Abbas[1,2] (✉), Ghulam Abbas[1], Waqas Zulfiqar[2,3], Muhammad Sajjad[1,4], Nirpendra Singh[4,5], and J. Andreas Larsson[1] (✉)

[1] *Applied Physics, Division of Materials Science, Department of Engineering Sciences and Mathematics, Luleå University of Technology, 97187 Luleå, Sweden*
[2] *Computational Materials Modeling Laboratory, Department of Physics, Government College University, Faisalabad 38040, Pakistan*
[3] *Department of Energy Conversion and Storage, Technical University of Denmark, 2800 Kgs. Lyngby, Denmark*
[4] *Department of Physics, Khalifa University of Science and Technology, Abu Dhabi-127788, United Arab Emirates*
[5] *Center for Catalysis and Separation (CeCaS), Khalifa University of Science and Technology, Abu Dhabi-127788, United Arab Emirates*

Received: 25 March 2022 / **Revised:** 9 May 2022 / **Accepted:** 8 June 2022

ABSTRACT

Anti-perovskites A_3SnO (A = Ca, Sr, and Ba) are an important class of materials due to the emergence of Dirac cones and tiny mass gaps in their band structures originating from an intricate interplay of crystal symmetry, spin–orbit coupling, and band overlap. This provides an exciting playground for modulating their electronic properties in the two-dimensional (2D) limit. Herein, we employ first-principles density functional theory (DFT) calculations by combining dispersion-corrected SCAN + rVV10 and mBJ functionals for a comprehensive side-by-side comparison of the structural, thermodynamic, dynamical, mechanical, electronic, and thermoelectric properties of bulk and monolayer (one unit cell thick) A_3SnO anti-perovskites. Our results show that 2D monolayers derived from bulk A_3SnO anti-perovskites are structurally and energetically stable. Moreover, Rashba-type splitting in the electronic structure of Ca_3SnO and Sr_3SnO monolayers is observed owing to strong spin–orbit coupling and inversion asymmetry. On the other hand, monolayer Ba_3SnO exhibits Dirac cone at the high-symmetry Γ point due to the domination of band overlap. Based on the predicted electronic transport properties, it is shown that inversion asymmetry plays an essential character such that the monolayers Ca_3SnO and Sr_3SnO outperform thermoelectric performance of their bulk counterparts.

KEYWORDS

electrical transport, anti-perovskites, low-dimensional materials, electronic structure, mechanical properties

1 Introduction

Until the discovery of two-dimensional quantum Hall effect (2D-QHE) [1], all phase transitions in crystalline materials could be explained well through Landau's theory of spontaneous symmetry breaking [2]. Since the integer Hall conductance in 2D-QHE arose without breaking any crystal symmetry, a new field of study in condensed matter physics came into existence based on the works of Thouless et al. [3] and Haldane [4], whereby transition between electronic states could be explained on the basis of topological phase transitions [5]. These pioneering works are now known to apply to a large range of 2D and three-dimensional (3D) materials and provide an effective tool for explaining phenomena beyond Landau theory. In the 2D realm, for instance, the experimental realization of monolayer (ML) graphene [6] has paved the way for the rapid advancement in synthesis and understanding of 2D materials, which were formerly considered to be thermodynamically unstable [2, 7]. Moreover, graphene also enabled the very first room temperature measurement of QHE resistance [8], showing that experimental and theoretical research efforts at the flat-land can be motivated for achieving diversification of physical properties in a 2D material that are not available in its 3D counterpart [9, 10]. As a result, we now have an extended family of 2D materials beyond elemental MLs [11–14].

In the backdrop of rapid discoveries in the 2D realm, little attention has unfortunately been paid to the 2D derivatives of perovskite-type materials, which are otherwise known to display a wide range of functional physical properties in their bulk form that are tunable to specific applications by manipulating their structure [15]. This can mainly be attributed to the fact that research efforts for 2D materials have been inspired by the mechanical exfoliation technique [16–18] and, therefore, exploring 2D layers of strongly bound bulk perovskites has remained a sort of "no-man's-land" since it is not possible to peel-off single layers. In addition, it was earlier believed that 2D limits of isotropically bonded perovskites are unachievable as a structural collapse below a critical film thickness of 5 unit cells (UC) would be triggered [19]. However, Ji et al. [20] successfully demonstrated that freestanding and structurally stable 2D $SrTiO_3$ and $BiFeO_3$

Address correspondence to Syed Muhammad Alay-e-Abbas, syed.muhammad.alay-e-abbas@ltu.se; J. Andreas Larsson, andreas.1.larsson@ltu.se

perovskites with high crystalline quality can be synthesized by adopting the synthesis technique developed by Lu et al. [21]. This layer-by-layer grow-and-release bottom-up technique has not only allowed the successful synthesis of other technologically important 2D perovskite oxides [22, 23], it has also encouraged theoreticians to employ first-principles calculations for exploring advanced structure–property relationships [24–27] that were previously untapped due to non-suitability of other top-down techniques for obtaining 1 UC thick 2D MLs of materials adopting the perovskite structure [20].

Apart from their technological importance for electronic and optical devices, 2D materials have also been extensively explored for applications in energy harvesting devices. A promising avenue for utilizing 2D materials in this context is their employment in thermoelectric (TE) devices which can help reduce the increasing global energy demands [28]. For example, graphene is one of the most thoroughly explored 2D materials due to its good mechanical strength, large surface area, and suitable electrical conductivity (σ) [29]. However, the semi-metallic nature of graphene leads to mediocre TE efficiency, for which various nano-level strategies have been proposed [30–32]. Unfortunately, these strategies fall short of being adopted for commercial purposes that have led researchers to explore other 2D materials for TE devices. Learning from the case of graphene where the opening of the band gap allows improvement in Seebeck coefficient (S) [33, 34], it is intuitive that oxide materials showing a semi-metallic nature, arising from a combination of crystal symmetry, spin–orbit coupling (SOC), and band overlap, in their bulk may lose these characteristics at the 2D limit. In particular, the anti-perovskite A_3SnO (A = Ca, Sr, and Ba) wherein the anions (Sn^{4-} and O^{2-}) and the cation (A^{2+}) occupy atomic sites inverse to those of a normal perovskite, are a unique class of solid materials that exhibit Dirac nodes in their electronic structure and are therefore good candidates for technologies requiring a vanishing band gap.

In the recent past, most of the theoretical and experimental research interest in anti-perovskites A_3SnO has mainly been motivated by trying to find an explanation behind the emergence of Dirac nodes in their band structure [35–45]. This has also led to the exploration of a wide array of structure–property relationships achievable in these materials, which give them flexible electronic, superconducting, and magnetic properties [46, 47]. Importantly, moderate values of S, low thermal conductivity (κ), and metallic nature of resistivity observed in experiments [43, 44] have also encouraged theoretical inquiry into their TE response [45]. While both the bulk and surface electronic states of normal ABO_3 perovskites show an insulating behavior [48, 49], the atomic arrangement of A_3SnO anti-perovskites can give rise to surface fermions that are attributed to the presence of inversion symmetry [39, 50–54]. The repulsion of conduction and valence band states for an electron precise A_3BO anti-perovskite [55] conventionally requires that a band gap should always be present near the Fermi level [56, 57]. However, because of an intricate interplay between crystal symmetry, SOC, and band inversion in the A_3BO compounds, an anti-crossing feature near the Γ symmetry point can be realized [40]. A vital feature arising out of the bands along the Γ–X path of an A_3BO anti-perovskite is the existence of symmetry protected Dirac nodes (Fig. 1(a)), which are influenced by SOC interaction and the degree of band inversion in A atom's d orbitals and Sn atom's p orbitals [52]. For instance, Ca and Sr containing anti-perovskites of Sn are trivial insulators and non-trivial topological crystalline insulators (TCIs), respectively [46, 58, 59]. On the other hand, Ba_3SnO (BSO) is predicted to be a topological semimetal exhibiting twin Dirac cones near the Fermi level [40].

Recent experiments employing molecular beam epitaxy (MBE) and pulsed laser deposition (PLD) techniques for the synthesis of A_3SnO thin films on various substrates indicate that (001)-oriented surfaces are experimentally achieved showing metallic character [44, 58, 60, 61]. These results also agree well with density functional theory (DFT) based first-principles calculation for the (001) surface [62–64]. Interestingly, it has become evident that manipulating the inversion symmetry in A_3SnO can significantly impact the evolution of the surface electronic structure [64]. Since A_3SnO surfaces in thin films are constructed by stacking $[A_2O]^{2+}$ and $[ASn]^{2-}$ layers along [001] direction, a net dipole moment perpendicular to the (001) would bring about an electronic reconstruction that gives rise to metallic states [62–64]. For the case of symmetric surface terminations (i.e., A_2O-terminated or ASn-terminated) studied for the bulk A_3SnO, electrons or holes from the bulk-like middle layer are available for electronic reconstruction to compensate for the polar catastrophe [64–66]. However, in the case of a 1 UC thick ML of A_3SnO, the absence of any bulk-like layer would result in a net electrostatic potential uncompensated by any electronic reconstructions when the band overlap is small. This scenario is depicted in Fig. 1, where one can see that for an asymmetric 2D system derived from the cubic space group #221 (*Pm-3m*) of bulk UC of Sr_3SnO anti-perovskite consisting of one Sr_2O and one SrSn termination (Fig. 1(b)), the resulting space group #99 (*P4mm*) lacks mirror symmetry as well as spatial inversion symmetry along the [001] direction. On the contrary, for a symmetric A_2O-terminated slab of anti-perovskites A_3SnO [62–64], both the inversion and mirror symmetries along [001] crystallographic direction are intact for the space group #123 (*P4/mmm*). Therefore, an opening of the band gap at the 2D limit may only be realized for the asymmetric MLs of A_3SnO. Notably, lifting the spatial inversion symmetry would also cause spin degeneracy in the electronic states to be lifted by SOC, giving rise to the emergence of Rashba-type splitting [64, 67, 68]. Since spin-dependent band splitting introduced by the Rashba-type spitting is directly associated with improvement in S, the opening of band gap in 2D MLs of A_3SnO suggests that better TE performance can be achieved in these systems [69].

2 Computational details

The dispersion-corrected DFT calculations in the present work are used for investigating the stability, electronic structure, and thermoelectric properties of A_3SnO-MLs (A = Ca, Sr, and Ba). If not otherwise noted, the calculations for structural,

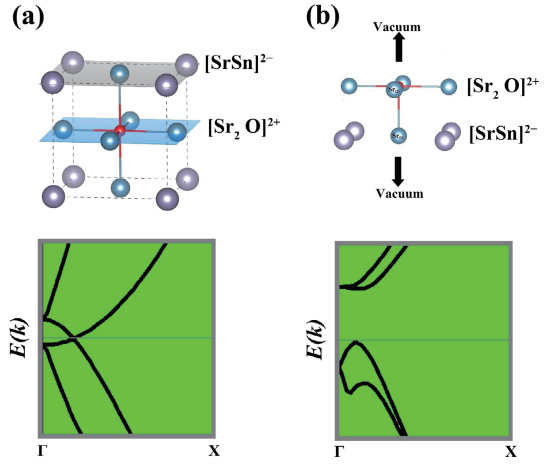

Figure 1 Schematic illustration of the band topology for the case of (a) bulk UC of Sr_3SnO and (b) 2D Sr_3SnO-ML along the Γ–X path. The cubic bulk UC of Sr_3SnO in (a) is constructed by stacking $[Sr_2O]^{2+}$ layer on top of a $[SrSn]^{2-}$ layer along all simply crystallographic directions. On the other hand, the 2D Sr_3SnO-ML is constructed by stacking one $[Sr_2O]^{2+}$ layer on top of one $[SrSn]^{2-}$ layer along the [001] direction followed by vacuum region. The Sr, Sn, and O atoms are represented by turquoise, gray, and red sphere.

thermodynamic, electronic properties, and transport properties of all bulk UC and 1 UC thick ML are performed using the all-electronic full-potential linear-augmented plane wave (FP-LAPW) method available in the WIEN2k code [70]. We have employed the BoltzTrap2 package [71] for computing the thermoelectric properties. On the other hand, the Vienna *ab-initio* simulation package [72] in combination with the Phonopy code [73] is employed to examine the dynamical stability. For the WIEN2k based calculations, we have set the muffin-tin radii of Ca, Sr, Ba, Sn, and O to 2.0, 2.2, 2.25, 2.3, and 1.8, respectively, and the plane wave cut-off is set to RK_{max} = 8.0. All the calculations are performed using an energy cut-off of –8.0 Ry to separate core and valance states, while a large value of G_{max} (24 $Bohr^{-1}$) is used. The bulk A_3SnO (A = Ca, Sr, and Ba) is first optimized for obtaining the ground state lattice parameters using an energy convergence criteria of 10^{-5} Ry. The ML systems are then derived from the bulk UC by introducing a vacuum region > 15 Å. These structural models are subsequently fully optimized using energy and force convergence criteria of 10^{-5} Ry and 1 mRy/a.u., respectively. For the bulk and 2D structural models of A_3SnO, we have employed 15 × 15 × 15 and 15 × 15 × 1 *k*-meshes, respectively. On the other hand, the electronic density of states (DOS) and transport properties are computed using 45 × 45 × 45 and 45 × 45 × 1 *k*-meshes, respectively. We note here that earlier DFT-based studies for the bulk UC of A_3SnO compounds report that a very dense *k*-mesh is necessary for obtaining a good approximation of the electronic density of states [45, 35]. However, despite the total energy convergence obtained with a shifted (a.k.a. "special" *k*-mesh) 15 × 15 × 15 *k*-mesh, the complex electronic structures of bulk A_3SnO compounds are not fully accessible. On the contrary, an unshifted 15 × 15 × 15 *k*-mesh is found to yield results in good agreement with a dense shifted or unshifted 45 × 45 × 45 *k*-mesh (Fig. S1 in the Electronic Supplementary Materia (ESM)). For this reason, in this study, we only present the electronic and transport properties computed using the unshifted *k*-mesh.

Since our calculations involve both bulk and 2D ML systems, the choice of DFT functional for a comparative analysis of the structural, thermodynamic, mechanical, and dynamical properties is crucial. While both generalized gradient approximation (GGA) and meta-GGA functionals are known to provide a good approximation of the physical properties of the bulk crystal, the inclusion of dispersion correction in these functionals does not necessarily work well for both worlds. In this context, the meta-GGA based SCAN + rVV10 functional is an exception that can simultaneously achieve a reliable account of the physical properties of both 3D and 2D realms [74, 75]. Our calculated results clearly show that inclusion of the dispersion correction through the rVV10 van der Waals (vdW) density functional [76] yields superior performance for structural and energetic properties of bulk A_3SnO compounds compared not only to previous calculations performed using the GGA-Perdew–Burke–Ernzerhof (PBE) functional [77] but also the bare SCAN meta-GGA. The SOC interactions in the A_3SnO systems are included through the second variational method [70] as these are necessary to capture the correct electronic structure of these materials. It is also worth mentioning here that recent DFT studies have demonstrated that SOC based electronic properties of A_3SnO compounds computed using the non-local modified Becke–Johnson (mBJ) potential functional [78, 79] are in better accord with experimental data compared to other approximations for the exchange-correlation potentials [45, 80]. Since a local modification of the mBJ potential functional designed for reproducing correct electronic properties of 2D materials better than the hybrid-DFT functionals has also recently been proposed [81, 82], we evaluate the electronic DOS, band structures, and transport properties of bulk UC and ML of A_3SnO systems using the semi-local and local modifications, respectively, of the mBJ potential functional.

3 Results and discussion

3.1 Structural, energetic, and thermodynamic properties of bulk A_3SnO

For a reliable account of the physical properties of bulk and ML modifications of A_3SnO systems, we begin our analysis by first evaluating the performance of SCAN + rVV10 exchange-correlation functionals of DFT in reproducing the structural and thermodynamic properties of the bulk systems. Although A_3SnO were first synthesized in the [83], little experimental data is available concerning the thermodynamic, dynamical, and mechanical stability of these compounds. However, only a couple of recent theoretical studies at the GGA-PBE level of DFT provide information about the thermodynamic stability of bulk A_3SnO compounds [64, 84, 85]. The better performance of the dispersion-corrected calculations in the present work compared to GGA-PBE and bare SCAN meta-GGA is evident from Figs. 2(a) and 2(b), where the reproducibility of the experimental data for the binary phases CaO, SrO, BaO, CaSn, SrSn, BaSn, Ca_2Sn, Sr_2Sn, and Ba_2Sn (Tables S1 and S2 in the ESM) computed using SCAN + rVV10 show smaller average absolute deviation in the ground state volume (0.237 $Å^3$/at.) and formation enthalpies (0.196 eV/at.). The better performance of SCAN + rVV10 approximation is further reflected in the good agreement of the calculated structural properties and the formation energies of bulk A_3SnO compounds (see Table S3 in the ESM). Moreover, the thermodynamic stability diagrams (details of the method adopted for computing stability diagrams are provided in Section S2 and S3 in the ESM) for the three A_3SnO compounds computed using SCAN + rVV10 (Fig. 2(d)) surprisingly show an almost overlapping stability region where similar values of the valid limits of the atomic chemical potentials of the Sn atom are obtained for the stable synthesis of bulk A_3SnO compounds. On the contrary, the atomic chemical potentials of Sn atom predicted by GGA-PBE (Fig. 2(c)) show a somewhat more dispersed range of the chemical potentials for these three compounds. Interestingly, the proximity of the stability line (I)–(IV) computed using SCAN + rVV10 functional for the three bulk A_3SnO compounds (restricting the formation of CaO, SrO, and BaO binary competing phases) is in excellent accord with experimental observation where better crystal quality as well as preclusion of AO phases is reported to be avoidable by a slightly excessive amount of alkaline-earth metal compared to what is stoichiometrically required for stable synthesis of these anti-perovskites [46].

3.2 Dynamical, and mechanical properties of bulk A_3SnO

Figures 3(a)–3(c) show the phonon band structures of the three bulk A_3SnO compounds computed with the SCAN + rVV10 functional where a 2 × 2 × 2 supercell is used. All three compounds are found to be dynamically stable in the cubic anti-perovskite structure as no imaginary phonon modes (indicated by negative frequencies in the phonon band structure) are observed at the Γ symmetry point. It is worth recalling here that $SrTiO_3$, a prototypical cubic perovskite oxide at room temperature, is known to undergo an anti-ferrodistortive phase transition at low temperature. From a theoretical stand point, this low temperature transition of $SrTiO_3$ is reflected in the imaginary phonon modes at the R symmetry point within the strongly-constrained and appropriately-normed (SCAN) based DFT calculations [86].

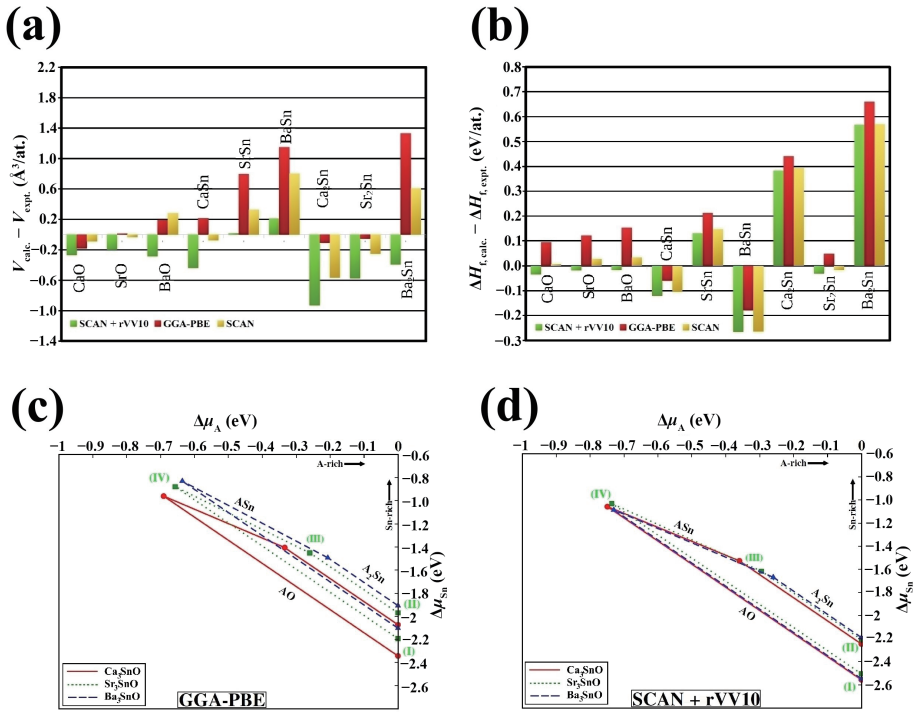

Figure 2 Deviation of the SCAN + rVV10, GGA-PBE, and bare SCAN meta-GGA functionals' (a) ground state volume per atom and (b) formation enthalpies per atom from the experiential data of CaO, SrO, BaO, CaSn, SrSn, BaSn, Ca_2Sn, Sr_2Sn, and Ba_2Sn binary compounds. (c) and (d) Show the thermodynamic stability regions of bulk UC of A_3SnO (A = Ca, Sr, and Ba) compounds computed using GGA-PBE data reported in Ref. [77] and SCAN + rVV10 in this work, respectively.

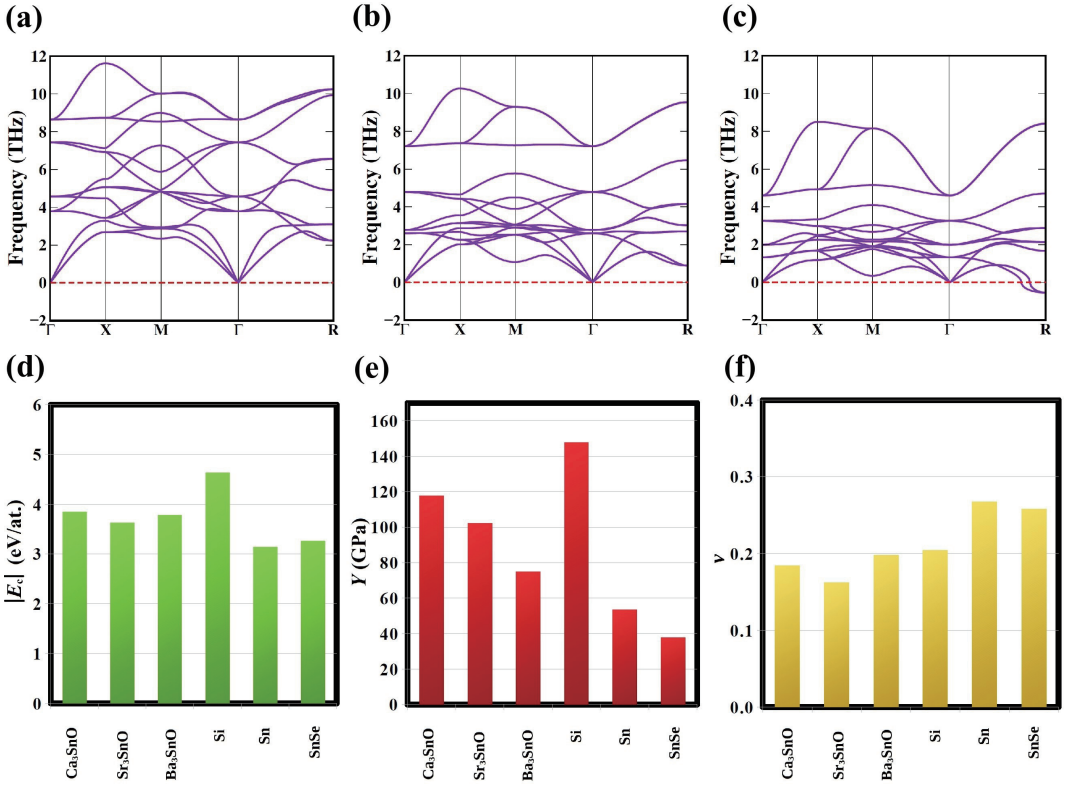

Figure 3 The phonon band structures of bulk UCs of (a) Ca_3SnO, (b) Sr_3SnO, and (c) Ba_3SnO compounds computed using SCAN + rVV10 parameterization scheme. In ((d)–(f)) we present the absolute value of $|E_c|$ (eV/at.), Y (GPa), and ν, computed using SCAN + rVV10. For bulk diamond UCs of Si and Sn, and orthorhombic UC of SnSe, the experimental [89] cohesive energies and GGA-PBE [90] mechanical properties are plotted for comparison.

Nevertheless, cubic perovskite structure of $SrTiO_3$ is dynamically stable under ambient conditions. Since a recent low temperature experimental study has shown that bulk Ba_3SnO undergoes a structural phase transition from the ideal cubic structure to an orthorhombic phase below 150 K [46], the negative phonon frequencies at the R symmetry point for bulk UC of Ba_3SnO in Fig. 3(c) are indicative of the reliable performance of SCAN + rVV10 calculations in predicting the dynamical properties of the three anti-perovskites studied in this work. This is further confirmed from the fact that both bulk UCs of Ca_3SnO and Sr_3SnO show no departure from the cubic *Pm-3m* phase at low temperatures [46].

Since cohesive energies and mechanical properties are commonly used for evaluating the stability of 2D materials [17],

for the sake of completeness we have also computed these values for the bulk UC of A_3SnO compounds. In Figs. 3(d)–3(f), we compare the cohesive energies ($|E_c|$), Young's modulus (Y), and Poisson's ratio (v) of the bulk A_3SnO compounds with bulk UCs of Si, Sn, and SnSe that are also potential TE materials at their 2D limit [17, 87]. It is evident from Fig. 3(d) that all the bulk A_3SnO compounds have larger cohesive energies than the bulk UCs of Sn and SnSe. These findings, together with the large negative formation enthalpies for Ca_3SnO (−9.207 eV/f.u.), Sr_3SnO (−8.676 eV/f.u.), and Ba_3SnO (−8.259 eV/f.u.) computed using the SCAN + rVV10 functional confirm the thermodynamic stability of these anti-perovskites. On the other hand, the SCAN + rVV10 calculated stiffness tensors (Table S4 in the ESM) confirm the mechanical stability (i.e. $C_{11} - C_{12} > 0$, C_{11}-2 × $C_{12} > 0$, $C_{11} > 0$, and $C_{44} > 0$) of the bulk A_3SnO compounds [88]. Comparison of Young's modulus presented in Fig. 3(e) clearly shows that the bulk UCs of A_3SnO compounds are less rigid than Si. The SCAN + rVV10 predicted Poisson's ratio of all three A_3SnO compounds are found to be smaller than those reported for bulk UCs of Si, Sn, and SnSe; indicating that a smaller transverse strain corresponding to linear strain may be observed in these materials. It is worth pointing out here that GGA-PBE predicts an auxetic behavior for bulk UC of Sr_3SnO [90]. In our SCAN + rVV10 calculations, on the other hand, no such behavior is seen for the three bulk UCs of A_3SnO compounds. All in all, the structural, thermodynamic, dynamical, and mechanical properties computed using the SCAN + rVV10 functional clearly show that this dispersion-corrected exchange-correlation parameterization scheme enables a better comparison with experimental data for bulk UCs of A_3SnO compounds.

3.3 Electronic properties of bulk A_3SnO

The electronic properties for the bulk UCs of three A_3SnO compounds computed using the SCAN + rVV10 functional indicate an anti-crossing feature along the Γ–X direction for both Ca_3SnO and Sr_3SnO. On the other hand, Ba_3SnO is found to exhibit a semi-metallic band structure with twin Dirac cones below the Fermi level along the Γ–X direction (Fig. S2 in the ESM). The electronic bands near the Fermi level computed using SCAN + rVV10 for Sr_3SnO and Ba_3SnO are qualitatively similar to the ones reported in earlier studies employing HSE06 and mBJ functionals [38, 40, 45, 52, 53, 84]. Since the applications of both the HSE06 hybrid functional [38] and the mBJ potential functional [45, 80] open up a band gap by slightly lifting the conduction band upwards along the Γ–X direction in bulk Ca_3SnO, in the present work, we focus mainly on the electronic properties predicted by the mBJ potential functional. In fact, electronic properties computed using the mBJ potential functional within the FP-LAPW method have already been shown to provide an excellent agreement with the band structures computed using the tight-binding model for the Wannier functions of the orbitals contributing near the Fermi level of bulk A_3SnO compounds [45]. Figure 4 presents the electronic band structure diagrams, and partial DOS plots of the bulk modifications of the three A_3SnO (A = Ca, Sr, and Ba) compounds computed using the mBJ parameterization scheme where one can see that the overlap of Ba-5d states and Sn-5p states in Ba_3SnO is the maximum below and above the Fermi level. In a recent study, we have performed a thorough analysis of differences in the ionic binding and metallic

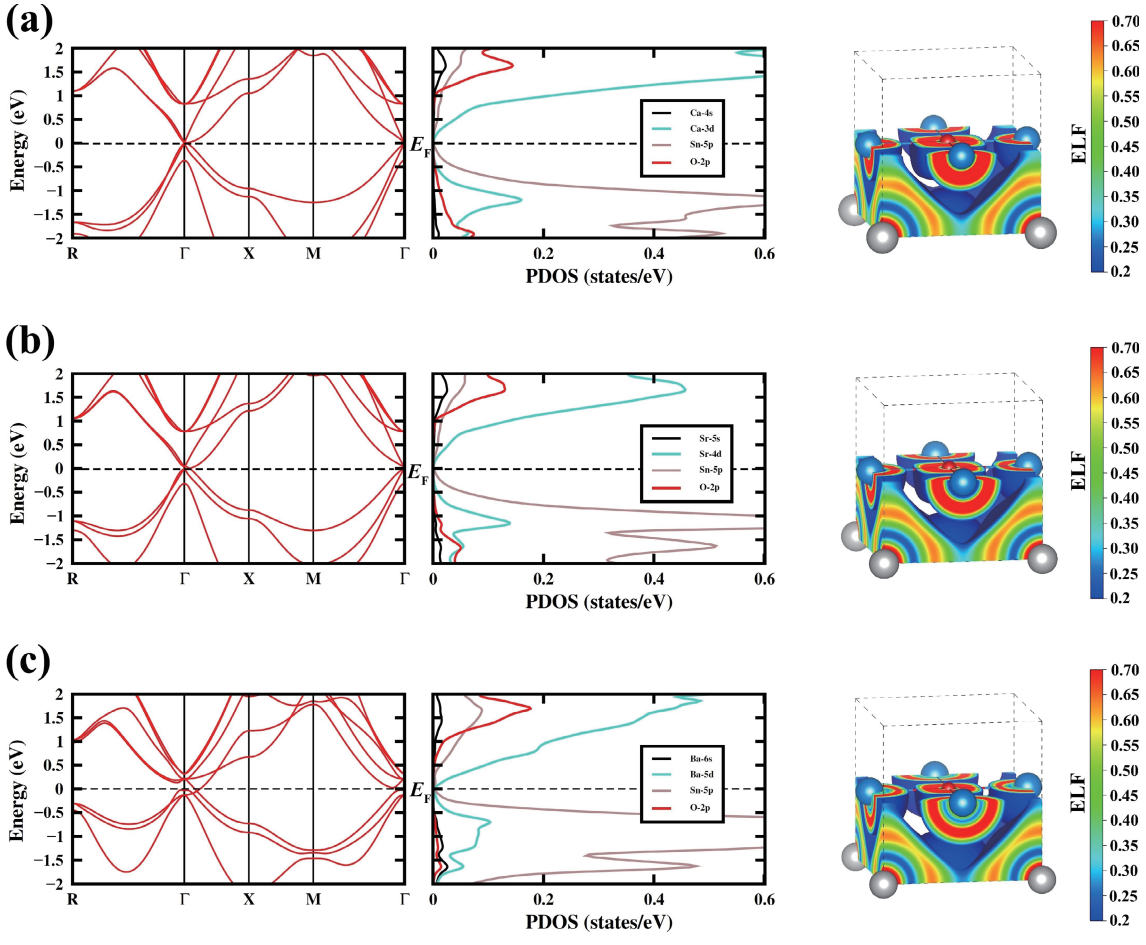

Figure 4 Electronic band structures (left panel) and partial density of states plots (middle panel) for bulk UCs of (a) Ca_3SnO, (b) Sr_3SnO, and (c) Ba_3SnO anti-perovskites computed using the non-local mBJ potential functional. The computed ELF for the three compounds within the 0.2–0.7 range are also shown in the right panel where an isosurface value of 0.2 is used (indicated by the blue colored surface) to show the changes in the metallic bonding between two Sn atoms in the ASn plane on going from Ca_3SnO to Ba_3SnO.

bonding in Ca_3SnO and Ba_3SnO [85], where smaller metallic interaction among Sn atoms in the BaSn layer of Ba_3SnO is found to be linked to the larger band overlap in this material. However, in order to compare the changes in the metallic bonding for three MLs derived from the bulk UCs of A_3SnO anti-perovskites (discussed later), we use the electron localization function (ELF) method of Becke and Edgecombe [91] for the structures optimized using the SCAN + rVV10 functional in the present study. Figure 4 again confirms the decreasing metallic interaction evident from the changes in the blue isosurfaces (corresponding to an ELF = 0.2 [92]) between two Sn atoms in the ASn layer on going from Ca_3SnO to Ca_3SnO. On the other hand, ionic binding [84, 85] between the A and O atoms in the A_2O layer is also confirmed. Since the partial DOS plots computed using the mBJ potential functional (Fig. 4) provide a reliable account of the competition between the SOC and band overlap in bulk UCs of A_3SnO compounds, it is evident that this functional provides an accurate description of the electronic properties of the bulk A_3SnO when combined with the structures computed using the dispersion-corrected SCAN + rVV10 functional [93].

3.4 Thermodynamic stability of A_3SnO-ML

For the three A_3SnO-ML (A = Ca, Sr, and Ba) systems studied in the present work, the phonon band structure for the fully optimized 1 × 1 × 1 vacuum supercell is shown in Figs. 5(a)–5(c), which have been computed using the SCAN + rVV10 functional. It is evident that all three anti-perovskite ML systems are dynamically stable and show no imaginary phonons modes along the X–Γ–M *k*-path. However, we note that small negative phonon frequencies emerge near the Γ point for larger (e.g., 3 × 3 × 1) supercells of Sr_3SnO-ML (see Fig. S3 in the ESM). Since we also found that the phonon band structure of a 2 × 2 × 1 supercell of $SrTiO_3$-ML calculated using SCAN + rVV10 exhibits imaginary phonon modes which disappear only for a 1 × 1 × 1 supercell, this can be due to the presence of electrostatic potential between A_2O and ASn layers whose influence enhances with increasing size of the supercell and cannot fall to zero for an infinite vacuum region [25, 94]. Similar negative phonon modes are also reported in earlier DFT studies for large supercell calculations of perovskite-type MLs [25, 27, 16]. To this end, we resort to further examining the thermodynamic stability of the A_3SnO-MLs that can be assessed in terms of the surface energy, γ, which should be a small positive value [16, 95–97]. However, due to the asymmetric surface termination, one can compute an averaged surface energy, $\widehat{\gamma}$, in terms of cleavage energy, β, which is defined as the energy required per unit area to create two free surfaces [97] and is given by the expression [96]

$$\beta = \frac{E^t_{A_3SnO\text{-}ML} - 3\left(E^t_A + \Delta\mu_A\right) - \left(E^t_{Sn} + \Delta\mu_{Sn}\right) - \frac{1}{2}\left(E^t_{O_2} + \Delta\mu_O\right)}{A} \quad (1)$$

In Eq. (1), $E^t_{A_3SnO\text{-}ML}$, E^t_A, and E^t_{Sn} and $E^t_{O_2}$ are the ground state energies of A_3SnO-ML, face-centered cubic (fcc) UCs of A = Ca, Sr, and Ba and diamond UC of Sn and an O_2 dimer computed using the SCAN + rVV10 functional. The atomic chemical potentials of A, Sn, and O in Eq. (1) are referenced to the thermodynamic stability diagram of bulk A_3SnO (Fig. 2(c)), while A is the surface area of the optimized A_3SnO-ML. It is worth noting here that writing cleavage energy in this way means that $\beta = 2\widehat{\gamma} = \gamma_1 + \gamma_2$; such that for a 2D system with symmetric surface terminations $\beta/2 = \widehat{\gamma} = \gamma_1 = \gamma_2$, while for an asymmetric 2D system such as A_3SnO-MLs studied here, $\beta/2 = \widehat{\gamma} \neq \gamma_1 \neq \gamma_2$. Therefore, the averaged surface energy for the A_3SnO-MLs studied in this work can be written as

$$\widehat{\gamma} = \frac{E^t_{A_3SnO\text{-}ML} - 3\left(E^t_A + \Delta\mu_A\right) - \left(E^t_{Sn} + \Delta\mu_{Sn}\right) - \frac{1}{2}\left(E^t_{O_2} + \Delta\mu_O\right)}{2A} \quad (2)$$

The $\widehat{\gamma}$ values for Ca_3SnO-ML, Sr_3SnO-ML, and Ba_3SnO-ML are found to be 0.942, 0.751, and 0.551 J/m^2, respectively, which are all

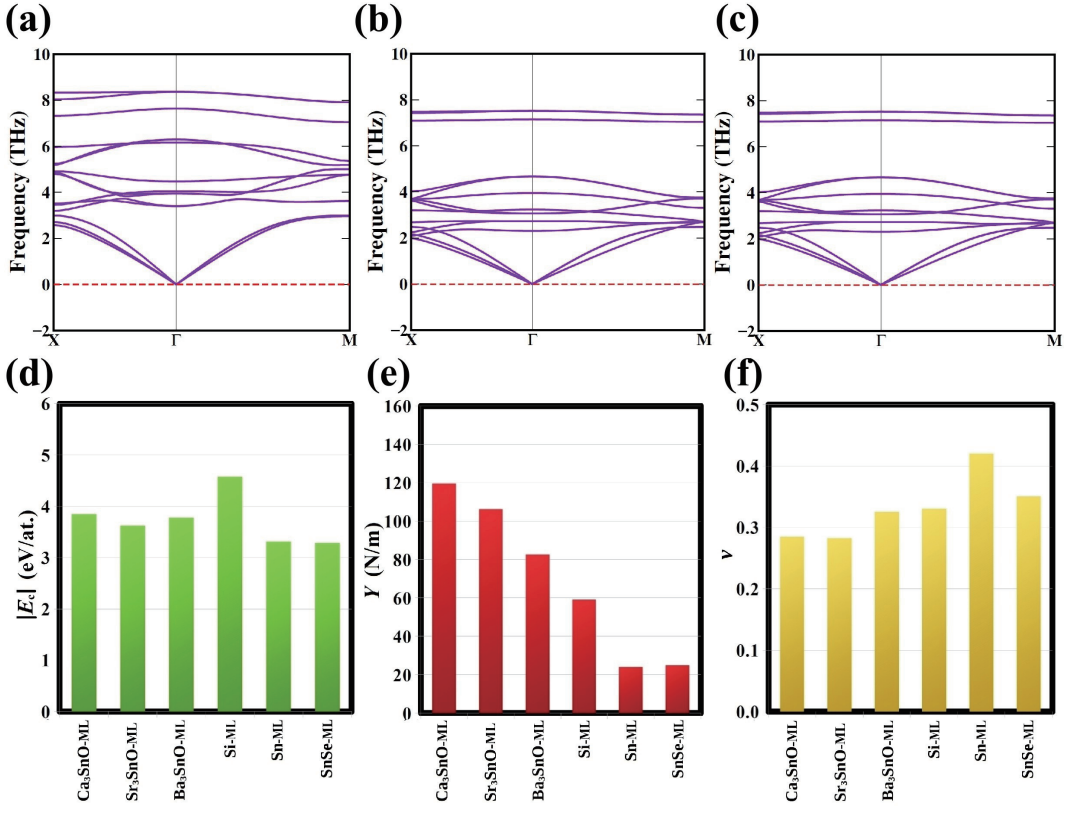

Figure 5 The phonon band structures of (a) Ca_3SnO-ML, (b) Sr_3SnO-ML, and (c) Ba_3SnO-ML systems computed using SCAN + rVV10 parameterization scheme. In ((d)–(f)) we compare the absolute value of $|E_c|$ (eV/at.), Y (N/m) and ν, computed using SCAN + rVV10. For Si-ML (silicene), Sn-ML (stanene), and SnSe-ML the theoretical data corresponding to zig-zag direction is plotted for comparison [17].

smaller than $\widehat{\gamma}$ = 1.206 J/m² which we have computed as a benchmark in the present work using the same procedure for a fully optimized 1 UC thick $SrTiO_3$-ML. Moreover, $\widehat{\gamma}$ of the studied ML systems are considerably smaller than surface energies of A_2O-termianted and ASn-terminated (001) surfaces of bulk A_3SnO [62, 63]. It is interesting to note that $\widehat{\gamma}$ for both asymmetric perovskite as well as anti-perovskite MLs decreases with increasing roughness of the surface (as discussed later). However, since all systems discussed here have a small positive value of $\widehat{\gamma}$, it is clear that these 2D ML systems are thermodynamically stable.

3.5 Structural, energetic, and mechanical properties of A_3SnO-ML

The stability of 2D A_3SnO-ML systems is also confirmed from the cohesive energies presented in Fig. 5(d), which are larger than the theoretical values of $|E_c|$ for stanene and SnSe-ML and comparable to the value of $|E_c|$ predicted for silicene [17]. Using the SCAN + rVV10 functional, we have also computed the stiffness tensors C_{11}, C_{22}, C_{12}, and C_{66} by transforming the 3D units (N/m²) to 2D units (N/m) (Table S5 in the ESM) where the mechanical stability of the three A_3SnO-MLs studied here is confirmed since all of $C_{11} > 0$; $C_{22} > 0$; $C_{66} > 0$; $C_{11} \times C_{22} - C_{12}^2 > 0$ are satisfied [88]. From Young's modulus presented in Fig. 5(e), it is evident that A_3SnO-MLs are slightly more rigid than silicene, stanene, and SnSe-ML. However, the Poisson ratios of the A_3SnO-ML are slightly enhanced compared to the bulk UCs of these systems, indicating that transverse strain corresponding to linear strain increases at the 2D limit of these anti-perovskites. However, the atomic structures of A_3SnO-MLs are anisotropic since in addition to shrink in the in-plane lattice parameters, the atomic positions diverge from their ideal limits in the bulk UCs of A_3SnO compounds. Figures 6(a)–6(c) show the in-plane $a_0 = b_0$ lattice parameters of the three A_3SnO-MLs, which have slightly shrunk compared to the lattice parameters of their corresponding bulk UCs (Table S3 in the ESM). Going from Ca_3SnO-ML to Ba_3SnO-ML, one can see that the upward shift of Sn atom from the ASn-layer and $A_{(2)}$ atom from the A_2O-layer increases. This is also evident from the increasing values of the displacement of Sn (i.e., Δz_{Sn}) and O (i.e., Δz_O) atoms relative to the $A_{(1)}$ and $A_{(2)}$ atoms, which result in the surface roughness. Such roughness has also been experimentally and theoretically observed in $SrTiO_3$-ML, $LaAlO_3$-ML, and $BiFeO_3$-ML, which is necessary for stabilizing a freestanding 2D system [20, 25]. To examine the in-plane variation of Young's modulus and Poisson's ratio relative to the x-direction, we have plotted the two quantities as a function in-plane angle θ in Figs. 6(d) and 6(e), respectively [98]. It is evident from Fig. 6(d) that the variation in Young's modulus does not exceed an increase of 30% compared to its values along the x-direction. On the other hand, the Poisson's ratio almost decreases to ~ 0 for Sr_3SnO-ML ($\nu(45°) = 0.064$) and Ba_3SnO-ML ($\nu(45°) = 0.095$) and even becomes negative for Ca_3SnO-ML $\nu(45°) = -0.002$), indicating that this 2D material might expand perpendicular to an in-plane stretch [17].

3.6 Electronic properties of A_3SnO-ML

The electronic properties of the A_3SnO-MLs computed using the local mBJ potential functional are presented in Fig. 7, where one can see that both Ca_3SnO-ML and Sr_3SnO-ML show an indirect band gap nature with small band gaps of 76 and 112 meV, respectively. The conduction band minima of both these ML systems are located at the Γ symmetry point, while the valence band maximum is found to be located slightly away from the Γ point owing to the emergence of Rashba-type splitting caused by the stronger influence of SOC interaction compared to the band overlap in these systems. On the other hand, the electronic band structure of Ba_3SnO-ML does not show splitting in the valence bands, while Dirac cones appear at the Γ symmetry point with a tiny mass gap of 29 meV. Although the electronic properties computed using the SCAN + rVV10 functional show all three ML systems to have almost similar electronic structure (Fig. S4 in the ESM), one can again see the better performance of the mBJ potential functional in reproducing the competition between SOC and band overlap for the bulk UCs of A_3SnO compounds reflected in the electronic structure of Ba_3SnO-ML. Since bulk UC of Ba_3SnO has a larger band overlap than Ca_3SnO and Sr_3SnO, a Rashba-type splitting in the valence band maximum is not seen in the electronic band structure of Ba_3SnO-ML [67, 69, 99].

Similar to the case of A_3SnO-ML studied in this work, Rashba-

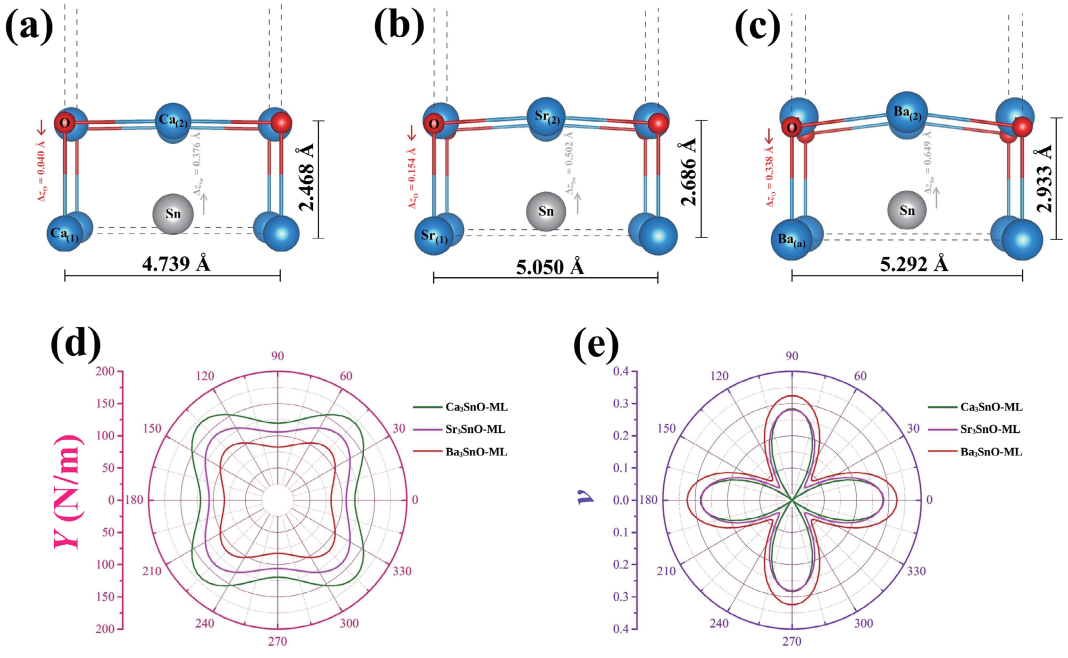

Figure 6 The fully optimized atomic structures of (a) Ca_3SnO-ML, (b) Sr_3SnO-ML. and (c) Ba_3SnO-ML systems having space group #99 (*P4mm*) showing the optimized in-plane lattice parameters and out-of-plane thickness along with the displacement of Sn (i.e., Δz_{Sn}) and O (i.e., Δz_O) atoms relative to the $A_{(1)}$ and $A_{(2)}$ atoms, respectively. (d) and (e) show Young's modulus and Poisson's ratio as a function of in-plane rotation angle θ.

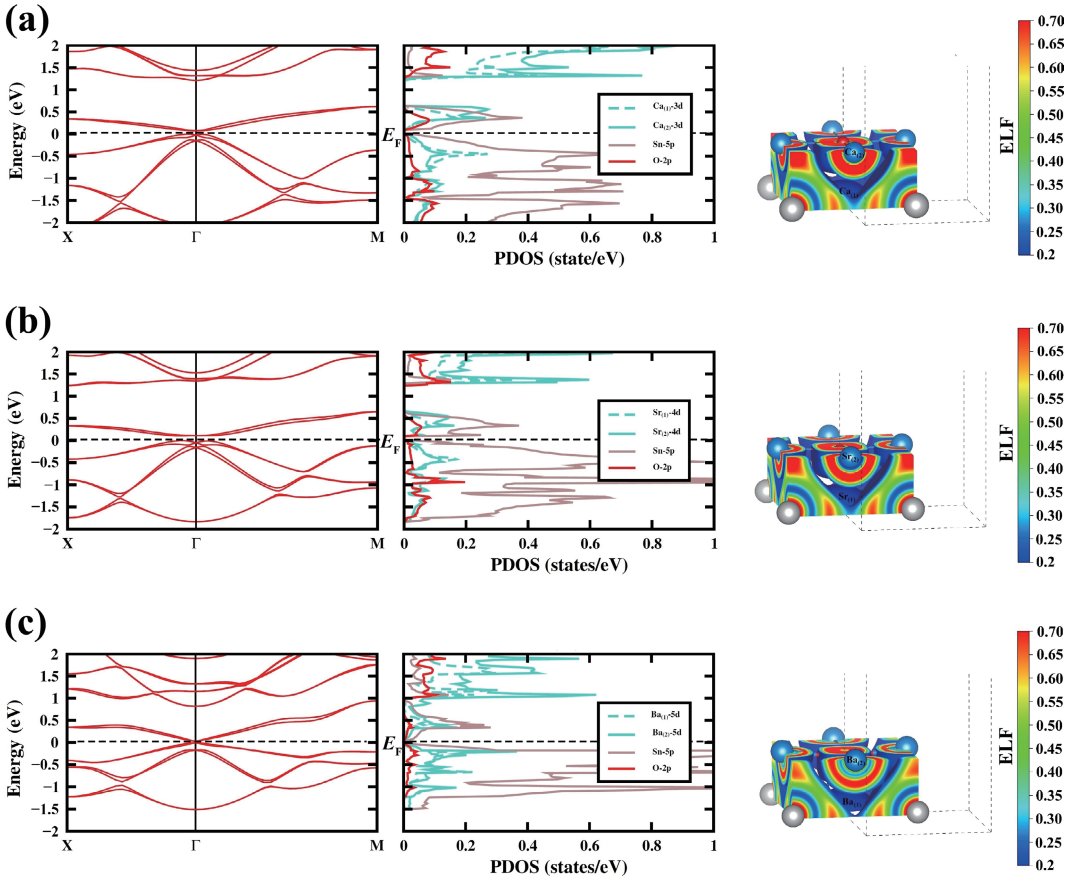

Figure 7 Electronic band structures (left panel) and partial density of states plots (middle panel) for 1 ML (a) Ca_3SnO, (b) Sr_3SnO, and (c) Ba_3SnO anti-perovskites computed using the local version of mBJ parameterization scheme. The computed ELF for the three ML systems within the 0.2–0.7 range is shown in the right panel where an isosurface value of 0.2 is used (indicated by the blue surface coloring) to show the changes in the metallic bonding between two Sn atoms in the ASn layer on going from Ca_3SnO-ML to Ba_3SnO-ML. For comparison, we show the ELF plots for that section of the ML system's structural model adopting space group #99 (*P4mm*) that can be directly compared with the ELF of bulk UC of A_3SnO anti-perovskite compounds displayed in Fig. 4.

type splitting in the electronic structure emerging due to the presence of inversion asymmetry has very recently been reported in experimental and theoretical studies carried out for other SOC dominated 2D perovskites [100, 101]. In order to examine the strength of the Rashba splitting evident in the electronic structures of Ca_3SnO-ML and Sr_3SnO-ML, we have computed the Rashba coefficient (α_R) using the expression

$$\alpha_R = 2E_R/k_R \quad (3)$$

where E_R is the energy difference between the band maximum and band degeneracy point (i.e. Γ symmetry point), and k_R is the momentum offset corresponding to these two energy values [102]. From the electronic band structures shown in Fig. 7, the Rashba coefficients for Ca_3SnO-ML and Sr_3SnO-ML are found to be 1.155 and 1.422 eV/Å, respectively. These values are clearly larger than other 2D systems [102] and comparable with the values reported for hybrid perovskites (1.6 eV/Å) [103] that are classified as conventional giant Rashba systems. It is worth mentioning here that the lifting of the band degeneracy caused by the asymmetric nature of the structural model or inclusion of SOC could result in the emergence of stable ferromagnetic (FM) ordering in A_3SnO systems [64, 84, 85]. This prospect is particularly important for the case of Ca_3SnO-ML and Sr_3SnO-ML systems studied in this work for which the emergence of Rashba-type splitting is caused by the stronger SOC and the presence of inversion asymmetry. By comparing the total energies of non-magnetic and FM calculations, we found an energy difference per surface area of < 0.1 eV/Å^2 and a zero spin magnetic moment for the relaxed A_3SnO-ML systems. This is also confirmed from the spin texture associated (Fig. S5 in the ESM) with the Rashba-type splitting observed in the electronic band structure of Sr_3SnO-ML (Fig. 7(b)) where the iso-energy in-plane S_x and S_y components involved in the valence band splitting near the Fermi level have opposite spin directions, which is a typical Rashba pattern [102].

It is evident from the projected density of states (PDOS) plots shown in Fig. 7 that the $A_{(1)}$ atom's d states contribute more in the valence band maximum than the $A_{(2)}$ atom's d states for Ca_3SnO-ML and Sr_3SnO-ML, resulting in the Rashba-type splitting and small band gaps. On the other hand, the $Ba_{(2)}$-5d states show a slightly larger contribution than $Ba_{(1)}$-5d states in the valence band maximum of Ba_3SnO-ML. Moreover, the unoccupied mid-gap bands above the Fermi level have larger contributions from Sn-5p states in Ca_3SnO-ML and Sr_3SnO-ML compared to an almost equal contribution of $Ba_{(2)}$-5d and Sn-5p states above the Fermi level in Ba_3SnO-ML. The smaller overlap of the $A_{(2)}$ atom's d states and Sn-5p causes the emergence of localized electrons at the A_2O surface of Ca_3SnO-ML and Sr_3SnO-ML, which is confirmed from the significant values of ELF (> 0.7) for these systems compared to the metallic bonding (0.2 < ELF < 0.7) for the in-plane ASn layer (Fig. S6 in the ESM). On the other hand, for the case of Ba_3SnO-ML, both in-plane and out-of-plane ELF remain in the range 0.2 < ELF < 0.7. Since the conservation of electron localization function in the 0.2 < ELF < 0.7 range for Ba_3SnO-ML indicates significant charge transfer between the $[Ba_2O]^{2+}$ and $[BaSn]^{2-}$ layers, we quantitatively compare the charge localization at the A_2O surfaces by examining the changes in the effective Bader charges of the $A_{(1)}$, $A_{(2)}$, Sn, and O atoms of the ML systems of A_3SnO in comparison to their bulk counterparts (Table S6 in the ESM). It is evident from the computed data that the effective Bader charges for $Ba_{(1)}$, $Ba_{(2)}$, and Sn atoms Ba_3SnO-ML show larger deviation from their bulk values, indicating electronic reconstruction for this system

that conserves ELF in the 0.2 < ELF < 0.7 range. On the other hand, smaller deviations of the Bader charges for Ca_3SnO-ML and Sr_3SnO-ML confirm smaller charge transfer between the $[A_2O]^{2+}$ and $[ASn]^{2-}$ layers at the 2D limit such that localized electrons at the A_2O surface are responsible for the Rashba-type splitting near the valence band maximum which is a necessary ingredient for improving the electronic transport properties in these systems.

3.7 Transport properties

Comparing the electronic band structures of bulk UC and ML shown in Figs. 4 and 7, respectively, one can already expect that the electronic transport properties of Ca_3SnO-ML and Sr_3SnO-ML may have enhanced at the 2D limit. To examine this from an application point of view, in Fig. 8 we compare the S, electronic conductivity (σ_e/τ), and electronic thermal conductivity (κ_e/τ) of the bulk UCs and 2D MLs of A_3SnO as a function of chemical potential at 300 K. It is important to point out here that for the σ_e/τ and κ_e/τ values presented in Fig. 8, the shortcoming of the BolzTrap2 package [71] in normalizing the results for the ML systems is accounted for by multiplying these distance dependent quantities with bulk lattice parameters of A_3SnO compounds and dividing by 1.5 (i.e., number of layers that can be accommodated along [001] direction of the conventional anti-perovskite UC) [104]. It is clear from Fig. 8 that S, σ_e/τ, and κ_e/τ for the Ca_3SnO-ML and Sr_3SnO-ML have increased near the Fermi level compared to the values computed for their bulk counterparts. As a result, both these systems show large values of the thermoelectric figure of merit ZT as high as ~ 0.8 at 300 K, which is due to the Rashba-type spitting in the valence band maximum and directly linked with the enhancement of S [69]. On the contrary, all the relevant transport parameters and ZT values for Ba_3SnO-ML system show insignificant change near the Fermi level compared to its bulk counterpart. Since bulk Ba_3SnO is stable in the cubic phase above 150 K [46], we should point out here that the thermoelectric properties for this system at low temperature may be influenced by structural changes. However, the larger band overlap in Ba_3SnO would still restrict the enhancement in thermoelectric response at the 2D limit.

Although our results clearly show enhanced thermoelectric performance for Ca_3SnO-ML and Sr_3SnO-ML compared to their bulk counterparts, it is important to note that the σ_e/τ and κ_e/τ presented in Fig. 8 are computed within the constant relaxation time approximation ($\tau = 10^{-14}$ s used in the present work) [71]. On the other hand, the Seebeck coefficient and figure of merit are independent of the relaxation time (typically in the range of $\tau = 10^{-14}$ to 10^{-15} [45] for bulk UC of A_3SnO). However, the former quantity depends both on the electronic and lattice thermal conductivity for a given temperature T according to the relation

$$ZT_{e,l} = \frac{\sigma S^2 T}{\kappa_e + \kappa_l} \quad (4)$$

Thus, for a realistic evaluation of the thermoelectric properties the contribution of lattice thermal conductivity in the figure of merit for the bulk US and ML systems studied in the present study is necessary. However, the evolution of the scattering process, lattice thermal conductivity, and relaxation times are beyond the scope of the present study since we are interested in the impact of lifting inversion symmetry on the electronic properties on going from bulk to 2D limit of the A_3SnO anti-perovskites. Nevertheless, it is crucial to provide solid evidence for the studied 2D systems to provide a rationale for motivating future experimental research efforts. To this end, we present the calculated values of $ZT_{e,l}$ in the temperature range of 50 to 300 K for both bulk UC and ML systems by assuming a carrier concentration of 1.5×10^{-19} and a lattice thermal conductibility of $\kappa_l = 2.0$ W/(m·K) that are based on the values reported in recent experiments for bulk Ca_3SnO and Sr_3SnO [43–45]. The values presented in Fig. 9 show that the calculated $ZT_{e,l}$ for bulk Ca_3SnO are in excellent agreement with the experimental figure of merit at 300 K reported in an earlier study [43]. For both Ca_3SnO-ML and Sr_3SnO-ML, the results presented in Fig. 9 suggest that the thermoelectric performance can be enhanced by as much as ~ 150 % in the 2D system for the same level of carrier concentration as already observed in undoped bulk A_3SnO [43, 44]. This shows that the emergence of a small band gap and Rashba-type splitting in 2D MLs derived from A_3SnO anti-perovskites can further enhance their technological importance. In addition to enhancement in the thermoelectric

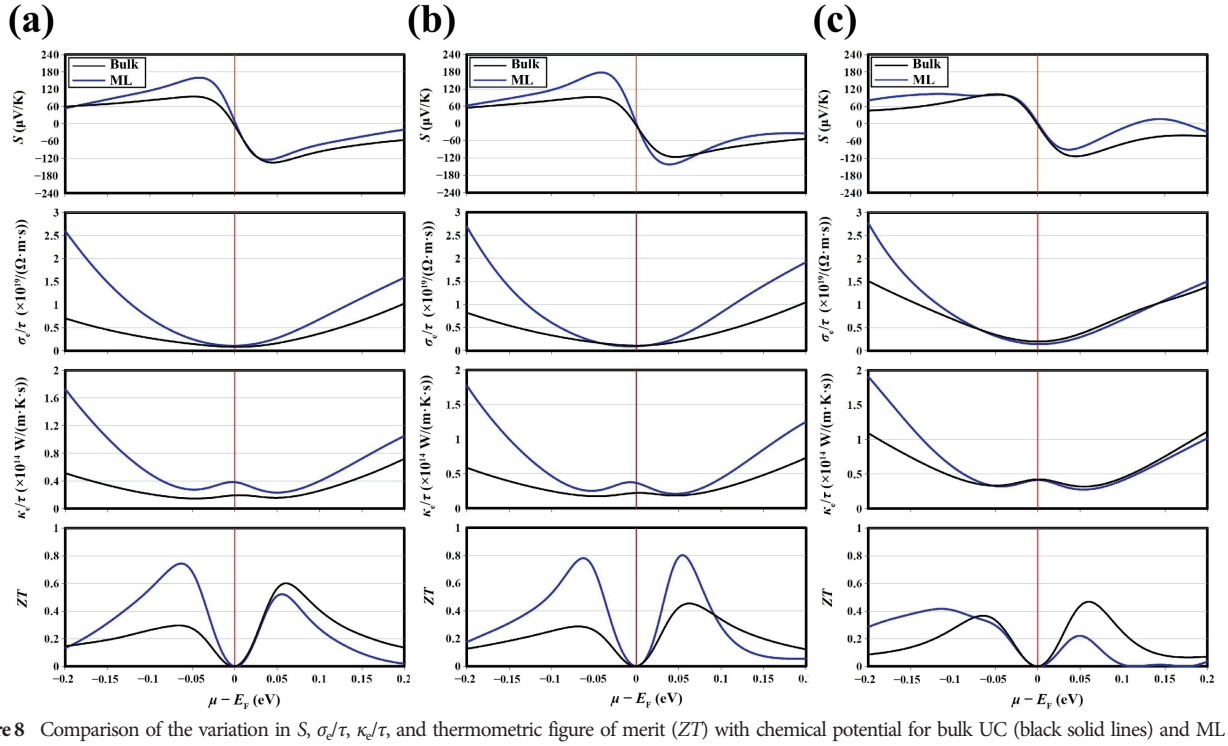

Figure 8 Comparison of the variation in S, σ_e/τ, κ_e/τ, and thermometric figure of merit (ZT) with chemical potential for bulk UC (black solid lines) and ML (blue solid lines) of (a) Ca_3SnO, (b) Sr_3SnO, and (c) Ba_3SnO at 300 K. All results have been computed using the mBJ potential functional.

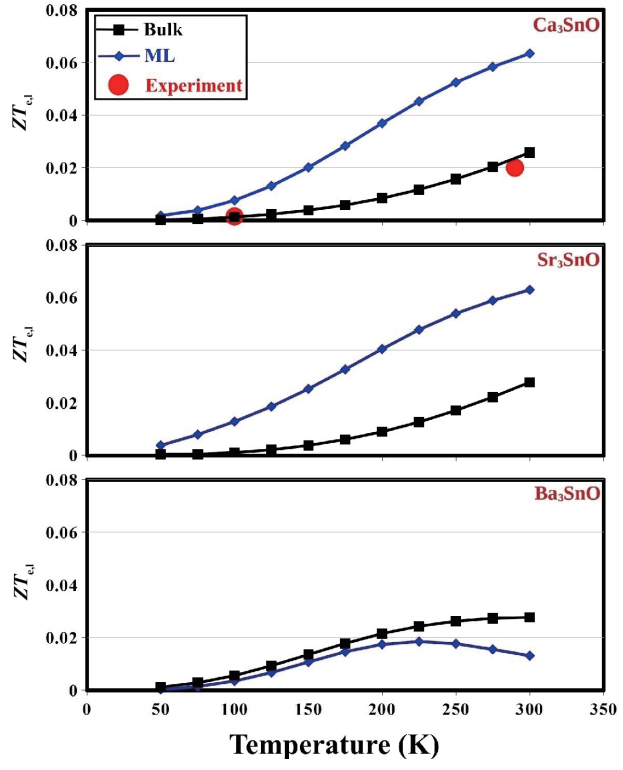

Figure 9 ZT_{el} vs. temperature for bulk UC (black solid lines) and ML (blue solid lines) of the A_3SnO systems in the temperature range of 50 to 300 K. The experimental data for bulk Ca_3SnO reported in Ref. [43] are shown as large red circles.

properties, the electronic structure of non-magnetic Ca_3SnO-ML and Sr_3SnO-ML also indicates the potential of these 2D systems for spintronic applications where the Rashba-type splitting introduced by the SOC can be manipulated with the application of an external electric field [99].

4 Conclusions

We have performed DFT calculations using reliable meta-GGA functionals to examine the impact of inversion asymmetry on the structural, thermodynamic, dynamical, mechanical, electronic, and thermoelectric properties of 1 UC thick MLs of the A_3SnO (A = Ca, Sr, and Ba) anti-perovskite. Our results clearly show the better performance of the SCAN + rVV10 in comparison with other exchange-correlation functionals by confirming the reproducibility of the experimental data for bulk UCs of relevant chemical systems with small average absolute deviation in the ground state structural and energetic properties obtained with this dispersion-corrected meta-GGA functional. Compared to GGA-PBE results, in particular, the SCAN + rVV10 calculations show that the stability region for the three A_3SnO compounds restricting the formation of CaO, SrO, and BaO binary competing phases have almost similar values of atomic chemical potential of Sn atom that yield stable formation of bulk systems, in agreement with experimental observation. In addition, the mechanical and dynamical properties predicted by SCAN + rVV10 functional for the bulk UCs of A_3SnO anti-perovskite show good accord with experiment. For obtaining a reliable picture of the electronic properties of bulk UCs of A_3SnO (A = Ca, Sr, and Ba) compounds, the electronic band structure, density of states, and transport properties are computed using the non-local mBJ potential functional. Comparison of the DOS and ELF computed for the bulk UCs of A_3SnO show that the decreasing metallic interaction among Sn atoms in the ASn layer. The increasing band overlap on going from Ca_3SnO to Ba_3SnO is responsible for closing of the band gap along Γ-X direction of the Brillouin zone. Since opening of the band gap at the 2D limit can be realized by removing the inversion symmetry at the 2D limit, we have also examined the structural, thermodynamic, dynamical and mechanical properties of A_3SnO-MLs by employing the SCAN + rVV10. Comparison of the calculated surface energies, phonon band structure, cohesive energies and mechanical properties with the values reported for silicene, stanene, SnSe-ML, and $SrTiO_3$-ML confirm the stability of the A_3SnO-MLs. The electronic properties computed using local mBJ potential functional indicate that Rashba-type splitting in the electronic structure emerges in Ca_3SnO-ML and Sr_3SnO-ML owing to strong spin–orbit coupling and inversion asymmetry in these systems. On the other hand, the Ba_3SnO-ML exhibits Dirac cone at the Γ symmetry point due to the dominance of band overlap in its electronic structure compared to spin–orbit coupling. By comparing the electronic transport properties of bulk and monolayer A_3SnO systems, we illustrate that the Rashba-type splitting caused by the presence of inversion asymmetry is responsible for significantly enhancing the thermoelectric properties in 2D anti-perovskites Ca_3SnO-ML and Sr_3SnO-ML.

Acknowledgments

S. M. A. A. and J. A. L. thank the Knut and Alice Wallenberg Foundation, and Kempestiftelserna for financial support. The computations were enabled by resources provided by the Swedish National Infrastructure for Computing (SNIC) at HPC2N and NSC partially funded by the Swedish Research Council through grant agreement no. 2018-05973.

Funding note: Open access funding provided by Luleå University of Technology.

Electronic Supplementary Material: Supplementary material (details of structural, thermodynamic, electronic and mechanical properties, phonon dispersion spectrum, spin components, ELF and Bader charges) is available in the online version of this article at https://doi.org/10.1007/s12274-022-4637-3.

References

[1] Klitzing, K. V.; Dorda, G.; Pepper, M. New method for high-accuracy determination of the fine-structure constant based on quantized hall resistance. *Phys. Rev. Lett.* **1980**, *45*, 494–497.

[2] Landau, L. D. Zur theorie der phasenumwandlungen II. *Phys. Z. Sowjetunion* **1937**, *11*, 26–35.

[3] Thouless, D. J.; Kohmoto, M.; Nightingale, M. P.; den Nijs, M. Quantized hall conductance in a two-dimensional periodic potential. *Phys. Rev. Lett.* **1982**, *49*, 405–408.

[4] Haldane, F. D. M. Model for a quantum hall effect without landau

levels: Condensed-matter realization of the "Parity Anomaly". *Phys. Rev. Lett.* **1988**, *61*, 2015–2018.
[5] Zou, J. Y.; He, Z. R.; Xu, G. The study of magnetic topological semimetals by first principles calculations. *npj Comput. Mater.* **2019**, *5*, 96.
[6] Geim, A. K.; Novoselov, K. S. The rise of graphene. *Nat. Mater.* **2007**, *6*, 183–191.
[7] Peierls, R. E. Quelques proprietes typiques des corpses solides. *Ann. Inst. Henri Poincare* **1935**, *5*, 177–222.
[8] Novoselov, K. S.; Jiang, Z.; Zhang, Y.; Morozov, S. V.; Stormer, H. L.; Zeitler, U.; Maan, J. C.; Boebinger, G. S.; Kim, P.; Geim, A. K. Room-temperature quantum hall effect in graphene. *Science* **2007**, *315*, 1379.
[9] Fiori, G.; Bonaccorso, F.; Iannaccone, G.; Palacios, T.; Neumaier, D.; Seabaugh, A.; Banerjee, S. K.; Colombo, L. Electronics based on two-dimensional materials. *Nat. Nanotechnol.* **2014**, *9*, 768–779.
[10] Novoselov, K. S.; Jiang, D.; Schedin, F.; Booth, T. J.; Khotkevich, V. V.; Morozov, S. V.; Geim, A. K. Two-dimensional atomic crystals. *Proc. Natl Acad. Sci. USA* **2005**, *102*, 10451–10453.
[11] Feng, B. J.; Zhang, J.; Zhong, Q.; Li, W. B.; Li, S.; Li, H.; Cheng, P.; Meng, S.; Chen, L.; Wu, K. H. Experimental realization of two-dimensional boron sheets. *Nat. Chem.* **2016**, *8*, 563–568.
[12] Glavin, N. R.; Rao, R.; Varshney, V.; Bianco, E.; Apte, A.; Roy, A.; Ringe, E.; Ajayan, P. M. Emerging applications of elemental 2D materials. *Adv. Mater.* **2020**, *32*, 1904302.
[13] Splendiani, A.; Sun, L.; Zhang, Y. B.; Li, T. S.; Kim, J.; Chim, C. Y.; Galli, G.; Wang, F. Emerging photoluminescence in monolayer MoS_2. *Nano Lett.* **2010**, *10*, 1271–1275.
[14] Zhao, W. J.; Ghorannevis, Z.; Chu, L. Q.; Toh, M.; Kloc, C.; Tan, P. H.; Eda, G. Evolution of electronic structure in atomically thin sheets of WS_2 and WSe_2. *ACS Nano* **2013**, *7*, 791–797.
[15] Ricciardulli, A. G.; Yang, S.; Smet, J. H.; Saliba, M. Emerging perovskite monolayers. *Nat. Mater.* **2021**, *20*, 1325–1336.
[16] Paul, J. T.; Singh, A. K.; Dong, Z.; Zhuang, H.; Revard, B. C.; Rijal, B.; Ashton, M.; Linscheid, A.; Blonsky, M.; Gluhovic, D. et al. Computational methods for 2D materials: Discovery, property characterization, and application design. *J. Phys. :Condens. Matter* **2017**, *29*, 473001.
[17] Hess, P. Bonding, structure, and mechanical stability of 2D materials: The predictive power of the periodic table. *Nanoscale Horiz.* **2021**, *6*, 856–892.
[18] Björkman, T.; Gulans, A.; Krasheninnikov, A. V.; Nieminen, R. M. Van der Waals bonding in layered compounds from advanced density-functional first-principles calculations. *Phys. Rev. Lett.* **2022**, *108*, 235502.
[19] Hong, S. S.; Yu, J. H.; Lu, D.; Marshall, A. F.; Hikita, Y.; Cui, Y.; Hwang, H. Y. Two-dimensional limit of crystalline order in perovskite membrane films. *Sci. Adv.* **2017**, *3*, eaao5173.
[20] Ji, D. X.; Cai, S. H.; Paudel, T. R.; Sun, H. Y.; Zhang, C. C.; Han, L.; Wei, Y. F.; Zang, Y. P.; Gu, M.; Zhang, Y. et al. Freestanding crystalline oxide perovskites down to the monolayer limit. *Nature* **2019**, *570*, 87–90.
[21] Lu, D.; Baek, D. J.; Hong, S. S.; Kourkoutis, L. F.; Hikita, Y.; Hwang, H. Y. Synthesis of freestanding single-crystal perovskite films and heterostructures by etching of sacrificial water-soluble layers. *Nat. Mater.* **2016**, *15*, 1255–1260.
[22] Han, L; Fang, Y. H.; Zhao, Y. Q.; Zang, Y. P.; Gu, Z. B.; Nie, Y. F.; Pan, X. Q. Giant uniaxial strain ferroelectric domain tuning in freestanding $PbTiO_3$ films. *Adv. Mater. Interfaces* **2020**, *7*, 1901604.
[23] Li, S. Y.; Zhang, Y.; Yang, W.; Liu, H.; Fang, X. S. 2D perovskite $Sr_2Nb_3O_{10}$ for high-performance UV photodetectors. *Adv. Mater.* **2020**, *32*, 1905443.
[24] Xue, Y. B.; Geng, C. H.; Guo, Y. Structural characterization and property modification for two-dimensional (001) $SrTiO_3$ nanosheets. *Appl. Nanosci.* **2020**, *10*, 4273–4279.
[25] Xiao, X. B.; Liu, B. G. Freestanding perovskite oxide monolayers as two-dimensional semiconductors. *Nanotechnology* **2021**, *32*, 145705.
[26] Liu, C.; Zhao, G. D.; Hu, T.; Bellaiche, L.; Ren, W. Structural and magnetic properties of two-dimensional layered $BiFeO_3$ from first principles. *Phys. Rev. B* **2021**, *103*, L081403.
[27] Chen, J. J.; Wu, K.; Hu, W.; Yang, J. L. Tunable Rashba spin splitting in two-dimensional polar perovskites. *J. Phys. Chem. Lett.* **2021**, *12*, 1932–1939.
[28] Vaqueiro, P.; Powell, A. V. Recent developments in nanostructured materials for high-performance thermoelectrics. *J. Mater. Chem.* **2010**, *20*, 9577–9584.
[29] Hsieh, Y. Y.; Zhang, Y.; Zhang, L.; Fang, Y. B.; Kanakaraaj, S. N.; Bahk, J. H.; Shanov, V. High thermoelectric power-factor composites based on flexible three-dimensional graphene and polyaniline. *Nanoscale* **2019**, *11*, 6552–6560.
[30] Yokomizo, Y.; Nakamura, J. Giant seebeck coefficient of the graphene/h-BN superlattices. *Appl. Phys. Lett.* **2013**, *103*, 113901.
[31] Chang, P. H.; Nikolić, B. K. Edge currents and nanopore arrays in zigzag and chiral graphene nanoribbons as a route toward high-*ZT* thermoelectrics. *Phys. Rev. B* **2012**, *86*, 041406.
[32] Juntunen, T.; Jussila, H.; Ruoho, M.; Liu, S. H.; Hu, G. H.; Albrow-Owen, T.; Ng, L. W. T.; Howe, R. C.; Hasan T.; Sun, Z. P. et al. Inkjet printed large-area flexible few-layer graphene thermoelectrics. *Adv. Funct. Mater.* **2018**, *28*, 1800480.
[33] Zuev, Y. M.; Chang, W.; Kim, P. Thermoelectric and magnetothermoelectric transport measurements of graphene. *Phys. Rev. Lett.* **2009**, *102*, 096807.
[34] Zhou, S.; Guo, Y.; Zhao, J. J. Enhanced thermoelectric properties of graphene oxide patterned by nanoroads. *Phys. Chem. Chem. Phys.* **2016**, *18*, 10607–10615.
[35] Nakamura, H.; Huang, D.; Merz, J.; Khalaf, E.; Ostrovsky, P.; Yaresko, A.; Samal, D.; Takagi, H. Robust weak antilocalization due to spin–orbital entanglement in Dirac material Sr_3SnO. *Nat. Commun.* **2020**, *11*, 1161.
[36] Huang, D.; Nakamura, H.; Takagi, H. Planar hall effect with sixfold oscillations in a Dirac antiperovskite. *Phys. Rev. Res.* **2021**, *3*, 013268.
[37] Huang, D.; Nakamura, H.; Küster, K.; Yaresko, A.; Samal, D.; Schröter, N. B. M.; Strocov, V. N.; Starke, U.; Takagi, H. Unusual valence state in the antiperovskites Sr_3SnO and Sr_3PbO revealed by X-ray photoelectron spectroscopy. *Phys. Rev. Mater.* **2019**, *3*, 124203.
[38] Hsieh, T. H. ; Liu, J. W. ; Fu, L. Topological crystalline insulators and Dirac octets in antiperovskites. *Phys. Rev. B* **2014**, *90*, 081112(R).
[39] Chiu, C. K.; Chan, Y. H.; Li, X.; Nohara, Y.; Schnyder, A. P. Type-II Dirac surface states in topological crystalline insulators. *Phys. Rev. B* **2017**, *95*, 035151.
[40] Kariyado, T. ; Ogata, M. Evolution of band topology by competing band overlap and spin–orbit coupling: Twin Dirac cones in Ba_3SnO as a prototype. *Phys. Rev. Mater.* **2017**, *1*, 061201(R).
[41] Fu, L. Topological crystalline insulators. *Phys. Rev. Lett.* **2011**, *106*, 106802.
[42] Fang, Y.; Cano, J. Higher-order topological insulators in antiperovskites. *Phys. Rev. B* **2020**, *101*, 245110.
[43] Okamoto, Y.; Sakamaki, A.; Takenaka, K. Thermoelectric properties of antiperovskite calcium oxides Ca_3PbO and Ca_3SnO. *J. Appl. Phys.* **2016**, *119*, 205106.
[44] Wu, W. Z.; Combs, N. G.; Stemmer, S. Molecular beam epitaxy of phase-pure antiperovskite Sr_3SnO thin films. *Appl. Phys. Lett.* **2021**, *119*, 161903.
[45] Ochi, M.; Kuroki, K. Comparative first-principles study of antiperovskite oxides and nitrides as thermoelectric material: Multiple Dirac cones, low-dimensional band dispersion, and high valley degeneracy. *Phys. Rev. B* **2019**, *12*, 034009.
[46] Nuss, J.; Mühle, C.; Hayama, K.; Abdolazimi, V.; Takagi, H. Tilting structures in inverse perovskites, M_3TtO (M = Ca, Sr, Ba, Eu; Tt = Si, Ge, Sn, Pb). *Acta Cryst. B* **2015**, *71*, 300–312.
[47] Leuenberger, M. N.; Loss, D. Spintronics and quantum computing: Switching mechanisms for qubits. *Phys. E:Low-Dimens. Syst. Nanostruct.* **2001**, *10*, 452–457.
[48] Zhu, G. Z.; Radtke, G.; Botton, G. A. Bonding and structure of a reconstructed (001) surface of $SrTiO_3$ from TEM. *Nature* **2012**, *490*, 384–387.
[49] Taylor, N. T.; Price, C. J.; Petkov, A.; Carr, M. I. R.; Hale, J. C.;

Hepplestone, S. P. The potential of overlayers on Tin-based perovskites for water splitting. *J. Phys. Chem. Lett.* **2020**, *11*, 4124–4130.
[50] Ando, Y.; Fu, L. Topological crystalline insulators and topological superconductors: From concepts to materials. *Annu. Rev. Condens. Matter Phys.* **2015**, *6*, 361–381.
[51] Teo, J. C. Y.; Fu, L.; Kane, C. L. Surface states and topological invariants in three-dimensional topological insulators: Application to $Bi_{1-x}Sb_x$. *Phys. Rev. B* **2008**, *78*, 045426.
[52] Kariyado, T.; Ogata, M. Three-dimensional Dirac electrons at the Fermi energy in cubic inverse perovskites: Ca_3PbO and its family. *J. Phys. Soc. Jpn.* **2011**, *80*, 083704.
[53] Kariyado, T.; Ogata, M. Low-energy effective Hamiltonian and the surface states of Ca_3PbO. *J. Phys. Soc. Jpn.* **2012**, *81*, 064701.
[54] Fuseya, Y.; Ogata, M.; Fukuyama, H. Spin-polarization in magneto-optical conductivity of Dirac electrons. *J. Phys. Soc. Jpn.* **2012**, *81*, 013704.
[55] Zintl, E. Intermetallische verbindungen. *Angew. Chem.* **1939**, *52*, 1–6.
[56] Huang, B. Q.; Corbett, J. D. $Ba_{21}Ge_2O_5H_{24}$ and related phases. *A corrected structure type and composition for a Zintl phase stabilized by hydrogen. Inorg. Chem.* **1998**, *37*, 1892–1899.
[57] Niewa, R. Alkaline-earth metal nitrides of the main-group elements: Crystal structures and properties of inverse perovskites. *Z. Anorg. Allg. Chem.* **2013**, *639*, 1699–1715.
[58] Lee, Y. F.; Wu, F.; Kumar, R.; Hunte, F.; Schwartz, J.; Narayan, J. Epitaxial integration of dilute magnetic semiconductor Sr_3SnO with Si(001). *Appl. Phys. Lett.* **2013**, *103*, 112101.
[59] Oudah, M.; Ikeda, A.; Hausmann, J. N.; Yonezawa, S.; Fukumoto, T.; Kobayashi, S.; Sato, M.; Maeno, Y. Superconductivity in the antiperovskite Dirac-metal oxide $Sr_{3-x}SnO$. *Nat. Commun.* **2016**, *7*, 13617.
[60] Ma, Y. J.; Edgeton, A.; Paik, H.; Faeth, B. D.; Parzyck, C. T.; Pamuk, B.; Shang, S. L.; Liu, Z. K.; Shen, K. M.; Schlom, D. G. et al. Realization of epitaxial thin films of the topological crystalline insulator Sr_3SnO. *Adv. Mater.* **2020**, *32*, 2000809.
[61] Minohara, M.; Yukawa, R.; Kitamura, M.; Kumai, R.; Murakami, Y.; Kumigashira, H. Growth of antiperovskite oxide Ca_3SnO films by pulsed laser deposition. *J. Cryst. Growth* **2018**, *500*, 33–37.
[62] Bilal, M.; Alay-e-Abbas, S. M.; Laref, A.; Noor, M.; Amin, N. First-principles investigations of structural, energetic and electronic properties of (001) surfaces of cubic inverse-perovskite Sr_3SnO. *J. Phys. Chem. Solids* **2020**, *136*, 109191.
[63] Bilal, M.; Alay-e-Abbas, S. M.; Sluydts, M.; Batool, J.; Laref, A.; Abbas, G.; Amin, N. DFT insights into surface properties of anti-perovskite 3D topological crystalline insulators: A case study of (001) surfaces of Ca_3SnO. *Phys. Lett. A* **2021**, *408*, 127469.
[64] Arras, R.; Gosteau, J.; Huang, D.; Nakamura, H.; Zhao, H. J.; Paillard, C.; Bellaiche, L. Spin-polarized electronic states and atomic reconstructions at antiperovskite $Sr_3SnO(001)$ polar surfaces. *Phys. Rev. B.* **2021**, *104*, 045411.
[65] Goniakowski, J.; Finocchi, F.; Noguera, C. Polarity of oxide surfaces and nanostructures. *Rep. Prog. Phys.* **2008**, *71*, 016501.
[66] Savoia, A.; Paparo, D.; Perna, P.; Ristic, Z.; Salluzzo, M.; Miletto Granozio, F.; Scotti di Uccio, U.; Richter, C.; Thiel, S.; Mannhart, J. et al. Polar catastrophe and electronic reconstructions at the $LaAlO_3/SrTiO_3$ interface: Evidence from optical second harmonic generation. *Phys. Rev. B* **2009**, *80*, 075110.
[67] Bychkov, Y. A.; Rashba, E. I. Properties of a 2D electron gas with lifted spectral degeneracy. *JETP Lett.* **1984**, *39*, 78–83.
[68] Nitta, J.; Akazaki, T.; Takayanagi, H.; Enoki, T. Gate control of spin–orbit interaction in an inverted $In_{0.53}Ga_{0.47}As/In_{0.52}A_{l0.48}$ as heterostructure. . *Phys. Rev. Lett.* **1997**, *78*, 1335–1338.
[69] Hong, M.; Lyv, W.; Li, M.; Xu, S. D.; Sun, Q.; Zou, J.; Chen, Z. G. Rashba effect maximizes thermoelectric performance of GeTe derivatives. *Joule* **2020**, *4*, 2030–2043.
[70] Blaha, P.; Schwarz, K.; Madsen, G. K. H.; Kvasnicka, D.; Luitz, J.; Laskowski, R.; Tran, F.; Marks, L. D. WIEN2k, an augmented plane wave + local orbitals program for calculating crystal properties. Karlheinz Schwarz, Techn. Universität Wien, Austria, 2018.
[71] Madsen, G. K. H.; Carrete, J.; Verstraete, M. J. BoltzTraP2, a program for interpolating band structures and calculating semi-classical transport coefficients. *Comput. Phys. Commun.* **2018**, *231*, 140–145.
[72] Kresse, G.; Joubert, D. From ultrasoft pseudopotentials to the projector augmented-wave method. *Phys. Rev. B* **1999**, *59*, 1758–1775.
[73] Togo, A.; Tanaka, I. First principles phonon calculations in materials science. *Scr. Mater.* **2015**, *108*, 1–5.
[74] Sun, J. W.; Ruzsinszky, A.; Perdew, J. P. Strongly constrained and appropriately normed semilocal density functional. *Phys. Rev. Lett.* **2015**, *115*, 036402.
[75] Peng, H. W.; Yang, Z. H.; Perdew, J. P.; Sun, J. W. Versatile van der Waals density functional based on a meta-generalized gradient approximation. *Phys. Rev. X* **2016**, *6*, 041005.
[76] Sabatini, R. ; Gorni, T. ; de Gironcoli, S. Nonlocal van der Waals density functional made simple and efficient. *Phys. Rev. B* **2013**, *87*, 041108(R).
[77] Kirklin, S.; Saal, J. E.; Meredig, B.; Thompson, A.; Doak, J. W.; Aykol, M.; Rühl, S.; Wolverton, C. The open quantum materials database (OQMD): Assessing the accuracy of DFT formation energies. *npj Comput. Mater.* **2015**, *1*, 15010.
[78] Tran, F.; Blaha, P. Accurate band gaps of semiconductors and insulators with a semilocal exchange-correlation potential. *Phys. Rev. Lett.* **2009**, *102*, 226401.
[79] Koller, D.; Tran, F.; Blaha, P. Merits and limits of the modified Becke–Johnson exchange potential. *Phys. Rev. B* **2011**, *83*, 195134.
[80] Tang, F.; Po, H. C.; Vishwanath, A.; Wan, X. G. Comprehensive search for topological materials using symmetry indicators. *Nature* **2019**, *566*, 486–489.
[81] Rauch, T.; Marques, M. A. L.; Botti, S. Local modified Becke–Johnson exchange-correlation potential for interfaces, surfaces, and two-dimensional materials. *J. Chem. Theory Comput.* **2020**, *16*, 2654–2660.
[82] Tran, F.; Doumont, J.; Kalantari, L.; Blaha, P.; Rauch, T.; Borlido, P.; Botti, S.; Marques, M. A. L.; Patra, A.; Jana, S. et al. Bandgap of two-dimensional materials: Thorough assessment of modern exchange-correlation functionals. *J. Chem. Phys.* **2021**, *155*, 104103.
[83] Widera, A.; Schäfer, H. Übergangsformen zwischen zintlphasen und echten salzen:Die verbindungen A_3BO (MIT A = Ca, Sr, Ba and B = Sn, Pb). *Mater. Res. Bull.* **1980**, *15*, 1805–1809.
[84] Batool, J.; Alay-e-Abbas, S. M.; Amin, N. Thermodynamic, electronic, and magnetic properties of intrinsic vacancy defects in antiperovskite Ca_3SnO. *J. Appl. Phys.* **2018**, *123*, 161516.
[85] Batool, J.; Alay-e-Abbas, S. M.; Johansson, G.; Zulfiqar, W.; Danish, M. A.; Bilal, M; Larsson, J. A.; Amin, N. Oxygen-vacancy-induced magnetism in anti-Perovskite topological Dirac semimetal Ba_3SnO. *Phys. Chem. Chem. Phys.* **2021**, *23*, 24878–24891.
[86] Zhang, Y. B.; Sun, J. W.; Perdew, J. P.; Wu, X. F. Comparative first-principles studies of prototypical ferroelectric materials by LDA, GGA, and SCAN meta-GGA. *Phys. Rev. B* **2017**, *96*, 035143.
[87] Li, D. L.; Gong, Y. N.; Chen, Y. X.; Lin, J. M.; Khan, Q.; Zhang, Y. P.; Li, Y.; Zhang, H.; Xie, H. P. Recent progress of two-dimensional thermoelectric materials. *Nano-Micro Lett.* **2020**, *12*, 36.
[88] Mouhat, F.; Coudert, F. X. Necessary and sufficient elastic stability conditions in various crystal systems. *Phys. Rev. B* **2014**, *90*, 224104.
[89] Kittel, C. *Introduction to Solid State Physics*; 8th ed. Wiley: New York, 2005; pp 105.
[90] Jain, A.; Ong, S. P.; Hautier, G.; Chen, W.; Richards, W. D.; Dacek, S.; Cholia, S.; Gunter, D.; Skinner, D.; Ceder, G. et al. Commentary: The materials project: A materials genome approach to accelerating materials innovation. *APL Mater.* **2013**, *1*, 011002.
[91] Becke, A. D.; Edgecombe, K. E. A simple measure of electron localization in atomic and molecular systems. *J. Chem. Phys.* **1990**, *92*, 5397–5403.
[92] Koumpouras, K.; Larsson, J. A. Distinguishing between chemical bonding and physical binding using electron localization function

(ELF). *J. Phys. :Condens. Matter* **2020**, *32*, 315502.
[93] Zulfiqar, W.; Alay-e-Abbas, S. M.; Abbas, G.; Laref, A.; Larsson, J. A.; Shaukat, A. Revisiting the structural, electronic and photocatalytic properties of Ti and Zr based Perovskites with meta-GGA functionals of DFT. *J. Mater. Chem. C* **2021**, *9*, 4862–4876.
[94] Radescu, S.; Machon, D.; Mélinon, P. Origin of dynamical instabilities in some simulated two-dimensional materials: GaSe as a case study. *Phys. Rev. Mater.* **2019**, *3*, 074002.
[95] Yang, Y.; Gao, F.; Gao, S. W.; Wei, S. H. Origin of the stability of two-dimensional perovskites: A first-principles study. *J. Mater. Chem. A* **2018**, *6*, 14949–14955.
[96] Pojani, A.; Finocchi, F.; Noguera, C. Polarity on the $SrTiO_3$(111) and (110) surfaces. *Surf. Sci.* **1999**, *442*, 179–198.
[97] Wang, L. X.; Lai, K. C.; Huang, L.; Evans, J. W.; Han, Y. Low-index surface energies, cleavage energies, and surface relaxations for crystalline NiAl from first-principles calculations. *Surf. Sci.* **2020**, *695*, 121532.
[98] Cadelano, E.; Palla, P. L.; Giordano, S.; Colombo, L. Elastic properties of hydrogenated graphene. *Phys. Rev. B* **2010**, *82*, 235414.
[99] Feng, Y.; Jiang, Q.; Feng, B. J.; Yang, M.; Xu, T.; Liu, W. J.; Yang, X. F.; Arita, M.; Schwier, E. F.; Shimada, K. et al. Rashba-like spin splitting along three momentum directions in trigonal layered $PtBi_2$. *Nat. Commun.* **2019**, *10*, 4765.
[100] Shao, Y.; Gao, W.; Yan, H. J.; Li, R. L.; Abdelwahab, I.; Chi, X.; Rogée, L.; Zhuang, L.; Fu, W.; Lau, S. P. et al. Unlocking surface octahedral tilt in two-dimensional ruddlesden-popper perovskites. *Nat. Commun.* **2022**, *13*, 138.
[101] Pham, M. T.; Amerling, E.; Ngo, T. A.; Luong, H. M.; Hansen, K.; Pham, H. T.; Vu, T. N.; Tran, H.; Whittaker-Brooks, L.; Nguyen, T. D. Strong rashba-dresselhaus effect in nonchiral 2D ruddlesden-popper perovskites. *Adv. Opt. Mater.* **2022**, *10*, 2101232.
[102] Lin, Z. Z.; Si, C.; Duan, S. R.; Wang, C.; Duan, W. H. Rashba splitting in bilayer transition metal dichalcogenides controlled by electronic ferroelectricity. *Phys. Rev. B* **2019**, *100*, 155408.
[103] Zhai, Y. X.; Baniya, S.; Zhang, C.; Li, J. W.; Haney, P.; Sheng, C. X.; Ehrenfreund, E.; Vardeny, Z. V. Giant Rashba splitting in 2D organic–inorganic halide perovskites measured by transient spectroscopies. *Sci. Adv.* **2017**, *3*, e1700704.
[104] Sajjad, M.; Singh, N.; Sattar, S.; De Wolf, S.; Schwingenschlögl, U. Ultralow lattice thermal conductivity and thermoelectric properties of monolayer Tl_2O. *ACS Appl. Energy Mater.* **2019**, *2*, 3004–3008.